Heterogeneity, Segmental and Hydrogen Bond Dynamics, and Aging of Supramolecular Self-Healing Rubber

Rongchun Zhang,[§] Tingzi Yan,[†] Bob-Dan Lechner,[†] Klaus Schröter,[†] Yin Liang,[‡] Baohui Li,[§] Filipe Furtado,[†] Pingchuan Sun,*[‡] and Kay Saalwächter*[†]

[†]Naturwissenschaftliche Fakultät II, Martin-Luther Universität Halle-Wittenberg, D-06099 Halle (Saale), Germany
[‡]Key Laboratory of Functional Polymer Materials, Ministry of Education, College of Chemistry, Nankai University, Tianjin 300071, P. R. China
[§]School of Physics, Nankai University, Tianjin 300071, P. R. China

ABSTRACT: In recent years, self-healing materials have attracted increasing attention due to their potentially spontaneous self-repairing ability after mechanical damage. Here, we focus on a supramolecular self-healing rubber based on fatty acids following the work of Leibler and co-workers. We study the heterogeneous network structure and hydrogen bond dynamics as well as its significant aging properties using several experimental techniques. NMR experiments reveal that the rubber is basically a two-component system, with a ~85% fraction of material rich in hydrogen-bonded structures and associated aliphatic moieties, undergoing a glass transition just below ambient temperature, and the other one being comprised of more mobile aliphatic chains. Changes in the IR bands corresponding to the NH bending and CO stretching vibrations show that water in the rubber not only takes the role of a plasticizer, reducing the glass transition temperature of the main component, but also is involved in changes of the hydrogen-bonding network. On the basis of shear rheology experiments and proton low-field NMR, we deduce that the rubber undergoes irreversible chemical cross-linking reactions at temperatures above 110 °C, going along with a weakening of its self-healing ability.
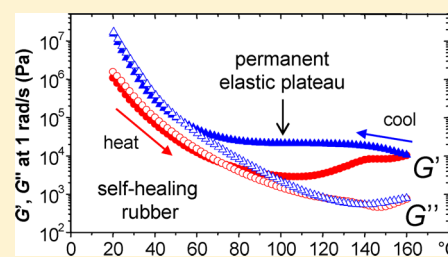
INTRODUCTION

In the past decades, synthetic polymers have completely changed our daily lives, being widely used in industry due to their low price, easy processing, and their exceptional physical and chemical properties. In addressing the new perspective, self-healing materials have attracted considerable recent attention due to their ability to autonomously and spontaneously repair themselves after suffering from surface or internal damage.[1−6] A traditional way of self-repair in resins is realized by embedding repairing chemicals in container capsules within the polymer matrix, initiating the chemical repair reactions by crack formation in the capsules.[7,8] In such systems, the chemical reaction can only take place once, and the mechanical properties of the material may be largely influenced or deteriorated by the presence of the capsules. Another elegant self-healing mechanism rests on the introduction of thermally reversible covalent bonds[9−11] or noncovalent supramolecular linkages[12] into polymers. In these materials, upon heating, the polymers can reversibly rupture and re-form to provide self-healing. Burnworth et al.[13] also synthesized an optically healable metallo-supramolecular polymer, which can convert photonic energy into localized heat, which in turn leads to healing via reversible dissociation of the metal-complex motifs. However, for these materials external energy is required for healing, which limits their application in industry.

Recently, Leibler and co-workers[2] synthesized a supramolecular rubber based on multivalent fatty acids, which is able to self-heal at room temperature without the need for external stimuli or embedding chemical substances into the polymer matrix. The self-healing ability was ascribed to a widespread hydrogen-bonding network formed by multifunctional oligomers carrying several associating hydrogen-bonding moieties. Upon fracture, tear, or abrasion, the network breaks by separation of the hydrogen-bonded moieties. As a result, a large number of free and active moieties located at the damaged surface can reassociate when the two surfaces are brought into contact again, thereby causing the interface to heal and the bulk structure to recover its original properties.[14] The resulting minimal-maintenance material may thus turn out to be of high economic relevance. This makes it necessary and important to improve our comprehensive understanding of the properties of this self-healing rubber (SHR).
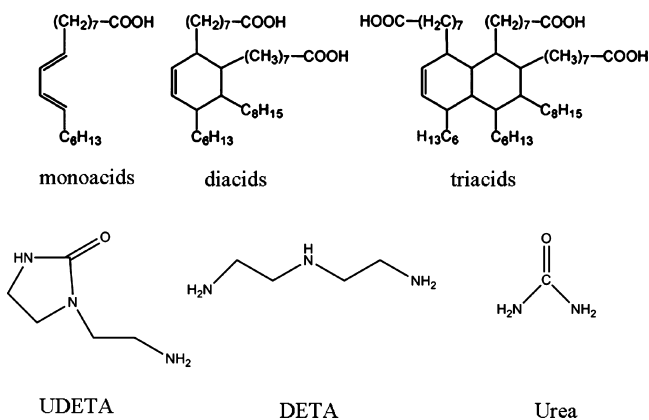
In this work, we focus on an SHR sample prepared by following the work of Leibler and co-workers,[15] investigating its heterogeneous structure, segmental and hydrogen-bond dynamics, and its aging behavior. We use different low- and high-field proton (^{1}H) NMR methods, IR spectroscopy, and shear oscillation rheology to study the material's properties on a molecular and macroscopic scale, respectively, and correlate these findings. Importantly, we demonstrate the material's

Scheme 1. Molecular Structure of the Raw Materials for SHR

Figure 1. DSC thermograms of the three SHR samples with T_g values indicated.

biphasic nature on the basis of NMR experiments that are sensitive to segmental motions and find that the material undergoes irreversible permanent cross-linking at temperatures above 110 °C, whereby its self-healing ability is compromised.

surface water by wiping just before the experiments. The DSC glass transition temperatures for the dried, ambient, and hydrated samples are about 289, 285, and 258 K, respectively, as shown in Figure 1. We note that the dried sample may not be completely water-free, but we wanted to avoid potential structural changes that may occur at higher drying temperatures (*vide infra*). As is apparent from the DSC thermogram in Figure 1, the glass transition of the hydrated sample takes place over a much wider temperature range, indicating significant inhomogeneity.

■ EXPERIMENTAL SECTION

Samples. The raw materials for the synthesis of SHR include a mixture of fatty mono-, di-, and triacids, diethylenetriamine (DETA), 2-aminoethylimidazolidone (UDETA), and urea, whose molecular structures are shown in Scheme 1. SHR was prepared according to published procedures,[15] which are shown in Scheme 2. The average number of COOH groups per molecule is n_{avg} = 2.03. We used fixed UDETA/DETA compositions, where x/n = 0.2 and y/n = 0.4. The successful synthesis was confirmed by reproducing many of the experimental results published in the related papers, using differential scanning calorimetry (DSC), X-ray diffraction, shear oscillation rheology, etc. A dried sample was obtained by storage in an oven under vacuum at 35 °C for about 2 days. For hydrated samples, we immersed the SHR in water (or D_2O) for about 2 days, removing the
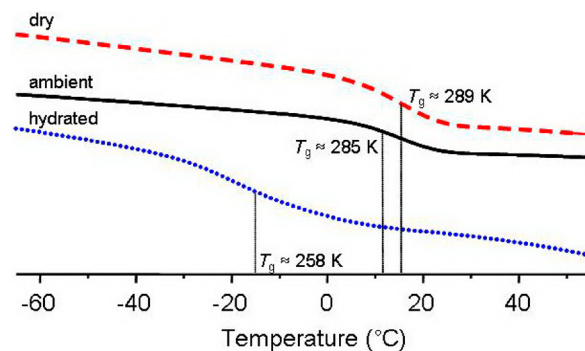
Infrared Experiments. Attenuated total internal reflection (ATR) IR experiments were performed with a Bruker BioATRII cell with Si internal reflective element on a Bruker Tensor27 using an MCT detector. Temperature was adjusted by a Haake Phoenix II thermostat (C25P, Thermo Electron Corporation, Karlsruhe, Germany) and controlled with a Delphi-based home-written software. Since the sample was densely pressed onto the ATR crystal within the sample well, air contact in the investigated area could be effectively avoided. The penetration depth of the IR irradiation is a function of the wavelength and can be estimated to be about 500−1000 nm in the investigated wavelength range.

Rheology. The dynamic shear modulus was measured at a frequency of 1 rad/s with an Anton Paar MCR 501 rheometer in the
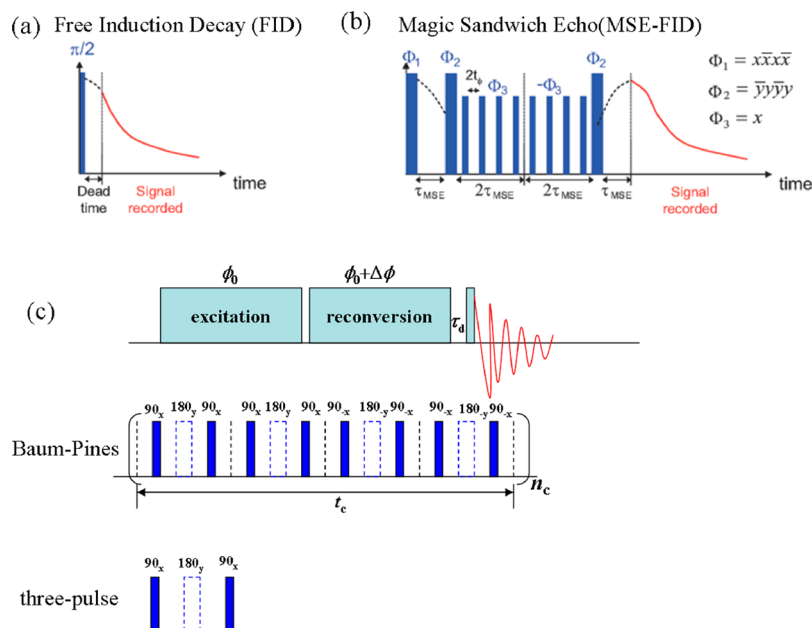
Scheme 2. Synthesis of SHR
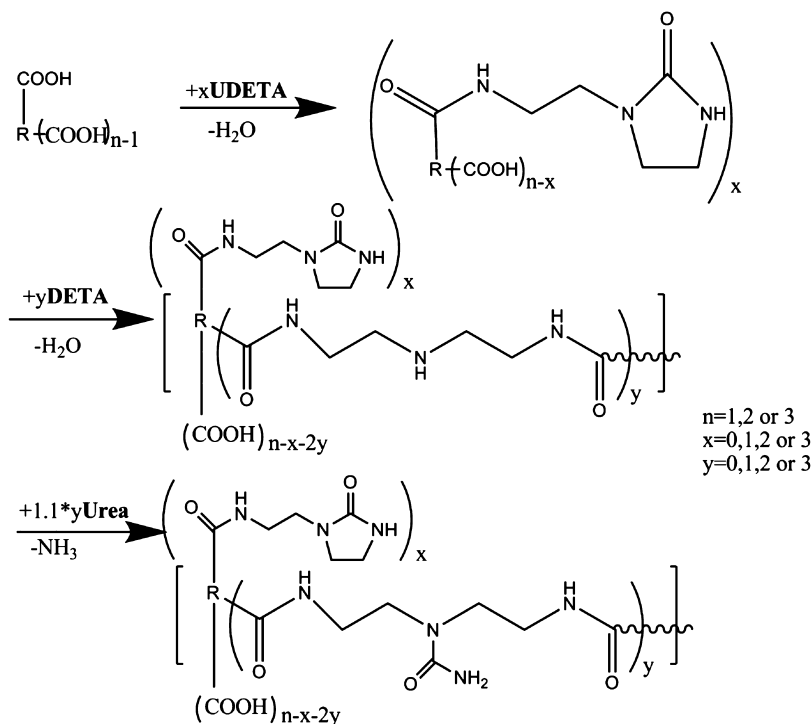
Figure 2. Pulse sequences. Solid bars denote 90° pulses, the open dashed bars denote 180° pulses, and the shaded areas represent groups of pulses. (a) Single-pulse excitation experiment for detecting the free induction decay (FID) signals, where the initial part is missing due to the dead time of the receiver. (b) Magic-sandwich echo (MSE) pulse sequence for refocusing the loss of rigid-phase signal due to the dead time. (c) Multiple-quantum (MQ) pulse sequence. The groups of pulses for the excitation and reconversion of higher spin coherences are the same except for their phases and can consist of the Baum–Pines or three-pulse segments, which both excite and reconvert double-quantum (and to a minor degree higher multiple-quantum) coherences.

linear-response range with strains of 0.5%. All measurements were done in parallel plate geometry with 8 mm diameter plates and a gap of around 1 mm. Temperature sweeps were measured from 20 to 160 °C with a temperature increment of 1 K/min. The samples were kept in a chamber under a nitrogen atmosphere.

Low-Field ^{1}H NMR. The measurements were performed on a Bruker Minispec mq20 low-field spectrometer at 20 MHz proton resonance frequency. The sample temperature was controlled with a BVT3000 heater working with a flow of heated air. In order to avoid O_2-related sample degradation, the NMR tube (10 mm outer diameter) was first flushed with nitrogen gas and then flame-sealed. The minispec has a typical $\pi/2$ pulse length of about 1.8 μs and a receiver dead time of about 11 μs.

Magic-Sandwich Echo Experiments. As the receiver of the minispec has a rather long dead time of 11 μs, the initial part of the free induction decay (FID) reflecting the rapidly decaying rigid-phase signals is missing, as shown in Figure 2a. This problem is tackled by the magic-sandwich echo (MSE) pulse sequence shown in Figure 2b.[16] Through adjusting the finite phase switching time t_ϕ of the instrument, the final echo time τ_{MSE} can be adapted to the receiver dead time, so as to almost fully recover the FID and its shape. In multiphase materials with different molecular mobilities, the FID can be well fitted with a combination of stretched or compressed exponential functions, $e^{-(t/\tau)^b}$. An exponent $b = 2$ (Gaussian) along with a very short (20–40 μs) τ indicates a rigid component, while $b \sim 1$ or even less (indicating a τ distribution) and longer τ indicate a potentially inhomogeneous components with fast mobility. Intermediate dynamics on the time scale of the inverse dipolar broadening of the rigid-limit spectrum ($\sim$20 μs) is reflected in apparent exponents between 2 and 1. In this range, more specific fitting functions apply,[17] as discussed below. In fully relaxed samples, using a sufficiently long recycle delay between individual scans, the NMR intensity is proportional to the total proton numer and inversely proportional to the Kelvin temperature according to the Curie law. In this way, the MSE-detected FID intensities were corrected, which allows to estimate intensity losses due to efficiency problems of the MSE related to intermediate mobility and other imperfections.[17,18]

Multiple-Quantum (MQ) NMR. For a complete account of the principle of MQ NMR as applied to polymers and soft materials we refer to ref 19. Pulse sequences of MQ experiments are shown in Figure 2c. Here we just recall the main procedures of the measurements as well as the data analysis. Depending on the phase cycle used, the MQ experiment yields two signal functions as a function of the double-quantum (DQ) evolution time τ_{DQ}, the decaying reference intensity (I_{ref}), and the double-quantum (I_{DQ}) buildup intensity. The sum of both form the sum MQ ($I_{\Sigma MQ}$) intensity, whose overall decay is dominated by the time scale of segmental orientation fluctuations, while the DQ intensity buildup at shorter times is governed by dipolar couplings between the many protons. These are strong ($D_{stat} \sim 30$ kHz) in a rigid/glassy system, while due to their orientation dependence they are reduced to zero in isotropic liquids or to a finite residual value (D_{res}) in cases of anisotropic mobility. The latter is realized by entanglement effects as well as cross-links in true networks, where fluctuations of the end-fixed subchains up to the milliseconds scale lead to a measurable anisotropy on the percent scale (as quantified by a dynamic order parameter $S \sim D_{res}$).[20] D_{res} is the main observable, and in actual rubbers it is proportional to the inverse network chain molecular weight ($D_{res} \sim 1/M_c$) and thus directly proportional to cross-link density.[20] The DQ intensity is subject to a relaxation effect at longer evolution time, which requires an intensity normalization protocol based upon a point-by-point division by the ΣMQ intensity

$$I_{nDQ} = \frac{I_{DQ}}{I_{\Sigma MQ}} \tag{1}$$

The normalization eliminates the effect of temperature-dependent segmental dynamics, so the normalized DQ intensity is exclusively dependent on D_{res} characterizing the structure of the rubber. However, before the normalization, the signal of usually slowly relaxing isotropically mobile components must be subtracted from the ΣMQ intensity, as shown in eq 2.

$$I_{\Sigma MQ} = I_{DQ} + I_{ref} - Be^{-2\tau_{DQ}/T_{2B}} - Ce^{-2\tau_{DQ}/T_{2C}} \tag{2}$$

B and C are the fractions of (in our case) two separable mobile components. For a very homogeneous system, after subtraction, the DQ intensity can be calculated and analyzed according to eq 3[21]

$$I_{nDQ}(\tau_{DQ}, D_{res}) = 0.5(1 - \exp\{-(0.378D_{res}\tau_{DQ})^{1.5}\})$$
$$\cos[0.583D_{res}\tau_{DQ}] \tag{3}$$

where D_{res} is the apparent residual dipolar coupling.

Generally, there are two most common excitation schemes for higher-spin coherences in static MQ experiments. One is the Baum–Pines segment,[22] and the other is the so-called three-pulse segment.[19,23] Both segments are shown in Figure 2c and induce DQ and higher-quantum transitions. In the relevant DQ buildup region, the signal is indeed dominated by double-quantum transitions only, making the experiments sensitive to apparent ^1H–^1H pair couplings. The most important difference between the two experiments is that the Baum–Pines segment is more robust at long times τ_{DQ} and can deal with a multiple-spin weak-coupling situation found in rubbers and melts far above the glass transition,[19] while the three-pulse segment suffers from efficiency problems in a multispin system but is more efficient when rather strong couplings are present (the minimum DQ evolution time is 10 μs as opposed to the ~100 μs minimum cycle time for the Baum–Pines segment). So in general, the three-pulse segment is usually adopted when materials with rather rigid regions are to be characterized.[22,24]

High-Field ^1H Magic-Angle Spinning (MAS) NMR. High-field experiments were performed on a Bruker Avance III 400 spectrometer, using a 4 mm double-resonance probe. The MAS frequency was set between 5 and 8 kHz. A 90° radio-frequency pulse of 3.5 μs was used on the ^1H channel. The chemical shift was referenced to external adamantane, whose proton chemical shift was set to 1.63 ppm. Proton single-pulse excitation and rotor-synchronized Hahn-echo experiments were performed for dry, ambient, and hydrated samples as well as for chloroform-swollen pristine and high-temperature aged SHR samples. Rotor synchronization means that the time intervals before and after the 180° pulse were set to integer multiples of the spinning period, which ensures that the results are free of rotor modulations. At moderate MAS rates, weak residual dipolar couplings among mobile protons are averaged out and the echo decay is long, while stronger couplings between multiple protons still lead to signficant dephasing and short apparent T_2 despite the MAS as a result of higher-order terms. This enables a similar yet somewhat qualitative mobility distinction as compared to static low-field NMR.

■ RESULTS AND DISCUSSION

Heterogeneous Structure and Segmental Dynamics. The SHR was claimed to exhibit an ordering at the nanometer scale arising from a segregation between unpolar and polar domains,[14] as suggested by X-ray scattering results.[2] The unpolar domains are rich in fatty acids, and the polar domains are rich in hydrogen-bonding moieties. The segregation of unpolar and polar domains reflects the heterogeneous structure of the SHR and possibly comes along with differences in molecular mobility in the different domains. In particular, the question arises whether the glass transition detected by DSC at around 287 K (ambient sample) may be related to only one of the two phases.

In principle, the molecular mobility can be investigated by studying simple FID signals. A fast decay indicates the presence of rigid components, while a slow decay corresponds to the response of mobile components. However, due to the dead time problem of the instrument, the acquired FID from single-pulse experiments will suffer from signal missing in the initial period which results in incomplete FID shapes. As the missing part corresponds to the response of very rigid components, it has to be retrieved. Herein, the MSE pulse sequence was used to recover the signal lost during the dead time. As shown in the
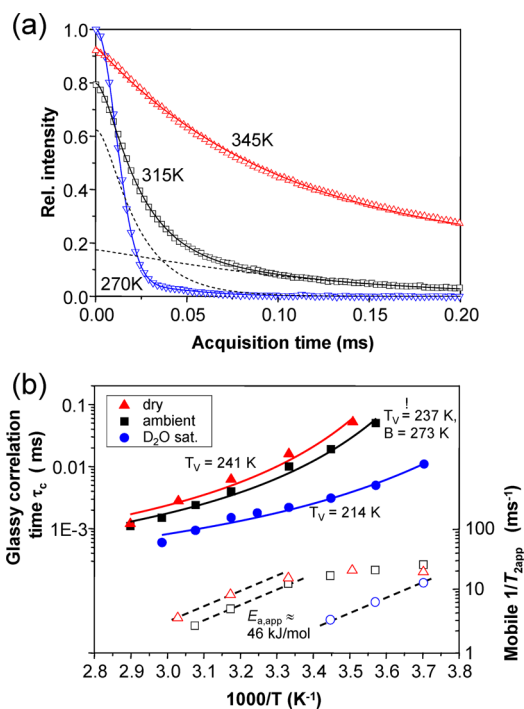

Figure 3. (a) MSE-refocused FID signals (for clarity with 7× reduced point density) as a function of the acquisition time for the dry SHR sample at three different temperatures. All intensities are corrected according to the Curie law. The two-component fitting curves are shown as solid curves, and separate components are shown as dashed curves for the 315 K data. (b) Log-scale plot of the correlation time τ_c obtained from the fit of the less mobile component (upper part) and the fitted mobile-component apparent $1/T_{2app}$ (lower part, excluding the highest-temperature values which are challenged by the shim limit) vs inverse temperature. The solid lines are fits to the Vogel–Fulcher equation, and the dashed lines are linear fits covering the high-temperature fast-motion region, yielding a constant apparent activation energy.

corresponding data for the dry sample in Figure 3, with increasing temperature, a motional-narrowing phenomenon is apparent, reflected in an increasingly slower decay of the signal traces. Note that the "NMR T_g", i.e., the temperature region where the most significant signal shape changes are observed, is located roughly 30–50 K above the calorimetric or hertz-scale dynamic glass transition, as the NMR signal is sensitive to fast motions on the 20 μs scale.

Previous work[17] has shown that the FID signal of a single polymer phase undergoing the softening transition above T_g can be well described by a function based on Anderson–Weiss (AW) theory.[25] The theory relies on a second-moment approximation of the distribution of the spectral frequency $\omega(\theta, \tau)$, and the ensemble- and time-averaged signal function reads

$$I_{FID}(t) = \langle\cos\int_t^{t+\tau}\omega(\theta, \tau)\rangle$$
$$= \exp\left[-M_2\tau_c^2\left(e^{-t/\tau_c} + \frac{t}{\tau_c} - 1\right)\right] \tag{4}$$

This result is based upon the assumption that the glass process can be described by an (almost) isotropic rotational diffusion process with correlation time τ_c, which should be related to the α relaxation time τ_α. M_2 is the dipolar second moment of the

rigid-limit (glassy) spectral line shape. The data in Figure 3 could not be fitted well to this function, indicating heterogeneity and additional components. We therefore chose a two-component fitting function, with an additional more mobile component modeled by a stretched/compressed exponential function, $e^{-(t/T_{2app})^b}$, to describe its decay:

$$I_{FID}(t) = A_g \exp\left[-M_2\tau_c^2\left(e^{-t/\tau_c} + \frac{t}{\tau_c} - 1\right)\right]$$
$$+ A_m e^{-(t/T_{2app})^b} \tag{5}$$

A_g represents the amplitude of glassy components that soften upon heating, and A_m denotes the mobile fraction. For the latter component we analyze the inverse decay time constant $1/T_{2app}$, corresponding to an apparent transverse relaxation rate. In the fast-motion limit (small τ_c), eq 5 exhibits an exponential limiting behavior with a relaxation rate $1/T_2 \approx M_2\tau_c$, so the T_{2app}^{-1} can be used to qualitatively asses the temperature dependence of the associated correlation time.

For the lower temperature range up to 325 K, the FID could be stably fitted using the above fitting function with all parameters free. From the fitting of the dry and ambient samples at $T = 270$ K, we found $M_2 = 8000$ ms^{-2} for the rigid limit, which was kept constant in all other fits. The mobile amplitude A_m was found to be constant in that range, corresponding to a fraction $A_m/(A_m + A_g)$ of about 15% in the dry and ambient samples. The stability of the fitting deteriorated at higher temperatures due to the limited acquired time window of 0.5 ms (and fitting longer times is not advised due to unknown signal shape related to field inhomogeneities rather than sample properties). Therefore, the amplitude A_m was kept fixed at all higher temperatures. Above 345 K the parameter b increased in an uncontrolled fashion and is fixed at a reasonable value of 2. This is the limit above which the intrinsic T_{2app} of the mobile fraction becomes longer than the decay related to the resolution (field inhomogeneity) of the magnet. In this range, the signal decay of a very mobile component indeed appears more or less Gaussian, and T_{2app} is in the milliseconds range, which means that the mobile component merely provides a plateau contribution to the intensity. So for 355 K and above, the amplitude A_g and the correlation time τ_c remained the only free variables in the fits.

For A_g we note an intensity minimum at 315 K (dry sample), which arises because the efficiency of the MSE before detection is compromised by the α process being in the intermediate dynamic range, corresponding to a T_2 minimum at the "NMR T_g".[17,18] The intensity minima for the ambient and hydrated samples were found at around 310 and 270 K, respectively, confirming the order of their respective T_gs. The correlation time τ_c could be fitted with the Vogel−Fulcher (VF) equation, $\ln \tau_c = \ln \tau_0 + B/(T - T_V)$, as shown in Figure 3b. The Vogel temperature was fixed at an estimated $T_g - 50$ K = 237 K for the ambient sample, determining B, and with B fixed, T_V of the dry and hydrated samples were estimated to 241 and 214 K, respectively, which again nicely reproduces the trend from the DSC values for T_g (Figure 1b). We take this finding as a proof of the validity of our fitting approach. We note that VF fits to the temperature-dependent shift factor obtained from frequency-dependent rheology results for the ambient sample (data not shown) yielded exactly the T_V estimated from the DSC T_g. This provides the overall confirmation that the

molecular dynamics in the majority phase dominates the mechanical behavior.

Upon cooling, the apparent relaxation rate $1/T_{2app}$ of the mobile component tends toward a plateau value (i.e., a lower T_2 limit). In the fast-motion high-temperature branch, an Arrhenius fit ($\ln cst/T_{2app} = \ln \tau_c = \ln \tau_0 + E_{a,app}/RT$; see the dashed line in Figure 3b) yields an apparent activation energy of about 46 kJ/mol describing the motion of the segments in this phase. From the data it is not possible to decide if a separate glass transition (Vogel−Fulcher behavior) exists in this domain, but notably, the segmental dynamics in this domain is obviously coupled to the majority component.

Summarizing, the main result of the FID component analysis is the observation that the more mobile components, which may have a T_g much below the DSC temperature ranges investigated so far, take up a (proton) fraction of around 15% of the samples, while the rigid fraction undergoing a glass transition somewhat below ambient temperature amounts to about 85% of the samples. The systematic error associated with ambiguities of the fitting procedure is estimated to around ±5%. Notably, the fitting quality was visibly inferior for the hydrated sample, which is consistent with its more pronounced dynamic inhomogeneity shown by DSC (Figure 1).

In order to assess the chemical nature of the two phases, we acquired ^{1}H high-resolution MAS spectra and introduced a rotor-synchronized Hahn echo to allow for a selective relaxation of the less mobile component (see Figure 4).
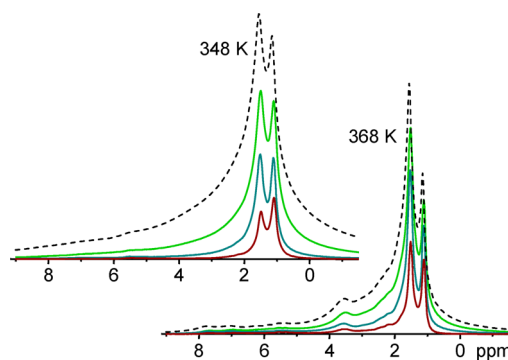

Figure 4. ^{1}H MAS spectra (8 kHz spinning frequency) of the ambient sample taken at two different temperatures far above T_g, acquired after a single pulse (dashed lines) and after rotor-synchronized Hahn echoes of duration 0.25, 1, and 2 ms.

Sufficiently resolved spectra could be taken around ∼350 K and above, where it is seen that the remaining component after a relaxation delay of 1−2 ms exclusively shows saturated alkyl resonances in the 1−2 ppm range. That means the saturated alkyl signals have the slowest decay rate, while the rigid hydrogen-bonding-related signals decay faster, which proves that the more mobile minority phase is hydrophobic in nature and is composed of long fatty-acid chains. Only at 370 K and above, the mobility of the less mobile majority phase is high enough to lead to resolved signals in the higher ppm range with sufficiently long T_2 to partially survive the Hahn echo filter.

The heterogeneous structure could be further addressed with MQ NMR experiments, as shown in Figure 5. The aim of these experiments was, initially, to reveal anisotropic mobility of chainlike structures, which would be evidence for entropic rubber elasticity.[19] This, however, requires heating of the samples to at least ∼70 K above T_g so as to have segmental
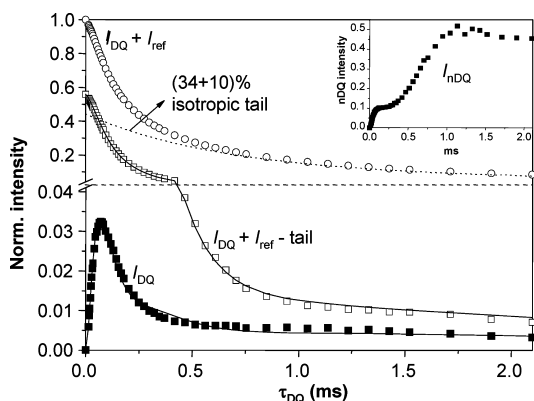
Figure 5. DQ buildup curve (solid squares) and sum intensity decay data (open circles) of dry SHR at 335 K. The solid curves are obtained from a simultaneous fit of the $I_{\Sigma MQ}$ decay (open squares, after tail subtraction) and I_{DQ} buildup signals. The normalized DQ buildup data are also shown in the inset.

Figure 7. Storage and loss moduli (G', G'') as a function of temperature at constant frequency of 1 rad/s and with a strain amplitude of 0.5% (for clarity with 5× reduced point density). The dry sample was first heated from 20 to 160 °C (red circles) and then cooled to 20 °C (blue triangles) with heating/cooling rates of 1 K/min.

mobility fast enough to minimize the overall signal relaxation (of the ΣMQ intensity) on the time scale of spin evolution due to small residual dipolar couplings (D_{res}). The aging at these temperatures (see below) prevented a consistent study of the pristine material, so we here focus at a temperature of $T = 335$ K, where aging is still slow but the α-relaxation is not yet fast on the NMR time scale. This implies rather large apparent D_{res} and requires the use of the three-pulse segment rather than the more stable Baum−Pines segment in the MQ experiment. The cycle time of the latter is too long, such that stronger coupled moieties are subject to dephasing due to higher-order terms in its average Hamiltonian.

The $I_{DQ} + I_{ref}$ decay data shown in Figure 5 reveal a biexponential tail, corresponding to about 44% isotropically mobile molecular segments, subdivided into a long-T_2 component of about 34%, which corresponds to the H-bonded mobile fraction identified above in the FID analysis, and another less mobile ∼10% fraction with a shorter T_2. The apparent mobile fraction is higher than in the FID component decomposition discussed above (34% vs 15%) because the relative intensity of the less mobile fraction is reduced due to intensity loss of the more rigid parts before MSE detection, as discussed above. The component fractions are thus not quantitative. The normalized DQ intensity curve as a function of DQ exciting time is shown in the inset of Figure 5. It reaches
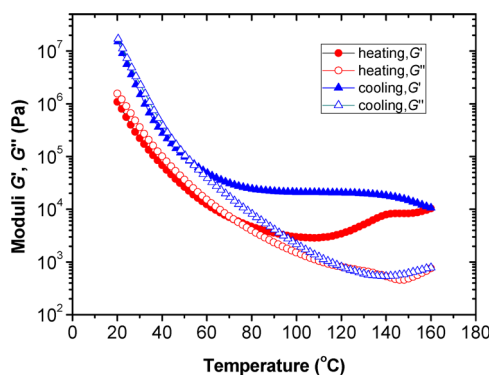
the theoretically expected plateau of 50% of the total intensity, and this observation represents a quality-control criterion for the reliability of the tail fit.[26] The nice two-step behavior suggests two subcomponents with different motional anisotropy (different D_{res}). However, this data could not be fitted with a combination of commonly used nDQ buildup functions such as eq 3, as the different components had different relaxation time,[27] which means that the point-by-point normalized DQ intensity is distorted.

Therefore, we resorted to a simultaneous fit of the raw DQ and ΣMQ signals, the latter after tail subtraction, as discussed in ref 27, taking explicitly into account the different relaxation behavior of the subcomponents. Again, a fit assuming a well-defined D_{res} for each subcomponent did not describe the data well, so we used a fit based on a Gamma distribution of couplings,[19] which is a generic function providing a good fit in heterogeneous scenarios,[28] but does not introduce a new fit parameter, as the distribution width depends on its average D_{av}:

$$P(|D_{res}|) = \frac{2}{\sqrt{\pi}} \sqrt{\frac{27|D_{res}|}{8D_{av}^3}} e^{-3|D_{res}|/(2D_{av})}$$

(6)

The total DQ buildup is calculated as a numerical finite-step integral according to
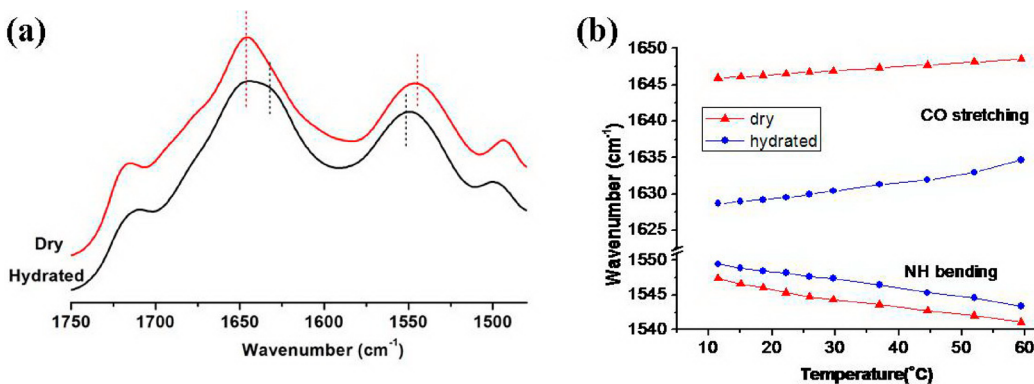

Figure 6. (a) ATR-IR spectra of the dry and hydrated samples at room temperature, with the relevant peaks marked by dashed lines. (b) The wavenumber of the N−H bending (around 1545 cm^{-1}) and the amide C=O stretching bands (around 1640 cm^{-1}) as a function of temperature for dry and hydrated SHR, restricted to <60 °C to prevent drying of the latter. The lines just guide the eye.

$$I_{DQ}(\tau_{DQ}) = \int P(D_{res}) I_{DQ}(\tau_{DQ}, D_{res}) \, dD_{res} \qquad (7)$$

using eq 3 as $I_{DQ}(\tau_{DQ}, D_{res})$ Kernel function. This distribution integration was used for each component in a simultaneous fit of I_{DQ} and $I_{\Sigma MQ}$ including empirical relaxation terms, following ref 27.

We could identify two majority components of roughly equal amplitude (demonstrating that the step height of the nDQ curve in the inset of Figure 5 is indeed somewhat distorted) with average D_{av} of 0.5 and 3 kHz, making up about 95% of the dipolar-coupled, less and anisotropically mobile component. This indicates that the main part of the sample undergoing the glass transition, made up of hydrogen-bonded moieties as well as parts of fatty acid chains as shown above (Figure 4), is again and not surprisingly substantially inhomogeneous. The SHR rubber is thus complex indeed. Note that this observation cannot be explained with the common dynamic heterogeneity of the glass transition in single-component systems,[29] as this phenomenon is restricted to the range of about 10 K above T_g.

We hesitate to further interpret the two different D_{av} values, as these may not so much reflect components of different anisotropic mobility in the long-time limit, but rather components with different α-relaxation time, which exhibit an only apparent residual orientation (anisotropic mobility) due to the closeness to T_g. The orientation correlations further decrease upon heating,[30] and we just note that the typical D_{res} values for entropically elastic rubber chains are in the 100 Hz range.[30] In the following, we will show that even at rather high temperature after aging, the fraction of chains that retain significantly anisotropic segmental dynamics is rather low, which is consistent with a rather low modulus in the rubbery plateau ($\sim 10^3 - 10^4$ Pa, depending on aging, as shown in Figure 7) as compared to "conventional" rubbers (where typically $G' \sim 10^5$ or larger). Thus, the elasticity of the SHR material is unconventional in a sense that the operation temperature of this rubber (room temperature) falls into the range of ongoing strong (molecular, thus also mechanical) relaxations. In other words, the SHR is not operated in the rubber elastic plateau range of the storage modulus, but within the strongly time- or frequency-dependent part toward the glass transition. This is directly apparent in the mechanical results discussed below.

Hydrogen-Bond Structure and Dynamics. Hydrogen bonds play an important role in determining the self-healing ability of the self-healing rubber, and there is a dynamic equilibrium between the association and dissociation of hydrogen bonds. With increasing temperature, the rates of dissociation and association increase, and the dynamic equilibrium is expected to shift toward the dissociated higher entropy state. Therefore, IR spectroscopy is a suitable probe for the investigation of qualitative changes in the hydrogen-bond structure and dynamics by observing potential wavenumber shifts of the vibrational band of the relevant hydrogen-bonding moieties as a function of temperature.[31−34] The ATR-IR spectra of the dry and hydrated samples at room temperature are shown in Figure 6a. We note two C=O stretching bands around 1640 cm^{-1} in the hydrated sample, one of which is at the same wavenumber position as in the dry sample, and another one at around 1630 cm^{-1}. As water may not interact with all C=O groups, we attribute the appearance of the new peak to C=O interacting with water. The wavenumber trend as a function of temperature is shown in Figure 6b and indicates significant changes with temperature and hydration level.

Table 1. Fitting Results (Average Residual Dipolar Couplings and Standard Deviations) from the DQ Buildup Curves in Figure 8

aged sample	$D_{av}/2\pi$ (Hz)	$\sigma/2\pi$ (Hz)
110 °C, ~1 h	423	141
160 °C, 5 h	120	40
160 °C, 8 h	83	28
160 °C, 21 h	75	27

With increasing temperature, the N−H bending band shifts to lower wavenumbers, while the C=O stretching band shifts to larger wavenumbers. Both shifts thus indicate H-bond dissociation, where in the dry sample, N−H···O=C hydrogen bonds should prevail. We note that for both signals water addition leads to shifts in wavenumber corresponding to sample cooling. Thus, while water may well replace the H-bonding partners on hydration, the relative direction of the wavenumber shift could indicate that the equilibrium is shifted to the closed state (while the dynamics may still be enhanced). We note that there is a variety of H-bond accepting sites in the sample (see also Scheme 2), explaining the high water absorption propensity of the SHR.[14] Equilibrium swelling experiments in water in fact revealed a swelling ratio (weight uptake) of about 1.20 of a dry sample.

We mention again the significant 30 K downward shift of T_g of the hydrated sample. This stresses that water absorption not only interferes with the H-bonds in the less mobile regions detected by time-domain NMR but also acts as a plasticizer, speeding up the overall molecular dynamics in that component.[2,14] It is remarkable that also the mobility of the phase-separated hydrophobic parts is enhanced, as can be inferred from the apparent T_2 times plotted in Figure 3b.

Aging. Initially, we set out to perform mechanical experiments to better understand the most application-relevant properties of the SHR and correlate them with our microscopic findings. Temperature-dependent oscillation rheology results are shown in Figure 7. We found that with increasing temperature the storage modulus of the dry sample decreased up to about 110 °C, above which it began to increase again, indicating a thermally irreversible aging process. This is proven by the cooling run back to 20 °C, where the storage and loss modulus are found to differ from the corresponding values obtained before heating. Notably, in the cooling run between 130 and 80 °C a pronounced plateau in G' becomes apparent.

The observation of the aging phenomenon is consistent with our failure to construct frequency-dependent master curves via frequency−temperature superposition at temperatures above about 90 °C, where the modulus changes in an irreversible fashion. Importantly, aged SHR samples exhibit a significantly weaker self-healing ability, providing an indication that a significant part of the physical H-bonds are replaced by chemical linkages. One could of course argue that this could also be due to the loss of bound water with increasing temperature, but this appears unlikely in view of the fact that the phenomenon was observed in a well-dried SHR.

To characterize the potential chemical network structure, Baum−Pines segment-based MQ experiments were performed at 110 and 160 °C. As mentioned above, 110 °C is the temperature above which chemical cross-link reactions speed up significantly, leading to a low degree of cross-linking during the temperature equilibration time (about 20 min) and the experimental time (about 1 h) of the MQ experiment. This is
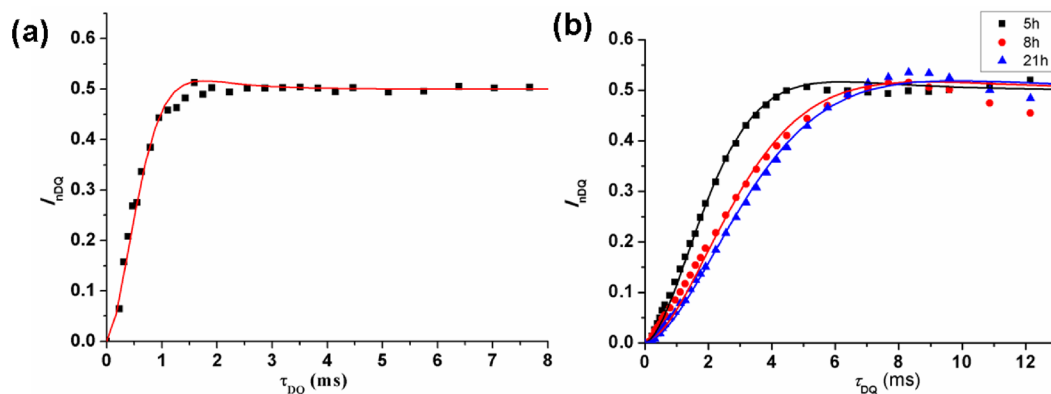
Figure 8. Normalized DQ intensity as a function of DQ evolution time at 110 °C (a) and 160 °C after different aging times (b), using the Baum–Pines segment. The nonelastic isotropic defect content taken from the subtraction of the tail of the $(I_{DQ} + I_{ref})$ data before normalization was about 95% for (a) and 65% for (b). The solid lines are fits on the basis of eq 7 with eq 3 as kernel function and a Gaussian distribution for $P(D_{res})$.[19−21] The fitting results are shown in Table 1, where D_{av} denotes the average residue dipolar coupling values and σ represents the distribution width.

indeed revealed by the normalized DQ buildup curve shown in Figure 8a, which demonstrates entropically active elastic chains comprising about 5% (proton integral) of the sample. Again, we stress that the majority of segments, whose motion appears still rather anisotropic at 70 °C (Figure 5), have become isotropically mobile above 100 °C on the milliseconds time scale of the MQ experiment.

Figure 8b shows nDQ buildup curves after variable aging times at 160 °C, where after 5 h of aging and above, 35% of the sample is made up of entropically elastic chains. Note that the time scale of changes in the sample in this late stage exceeds the time needed to perform a single MQ experiment. Interestingly, with further increasing aging time, the slope of the nDQ buildup curves, and therefore the (average) residual coupling D_{res} is reduced somewhat and reaches a constant value beyond 8 h of aging. This result indicates a complex multistep aging process during which the elastically active chains appear to be rather short in the beginning and equilibrate to a longer or relaxed state beyond 8 h of aging. In the final state, we observe a rather homogeneous system with uniform $D_{res}/2\pi = 75$ Hz, which in this case reflects a rather uniform average inverse molecular weight of a chain between actual cross-links.

The NMR results in Figure 8b reflect subtle changes during the late stage of aging, while the early stage buildup of the 35% fraction of entropically elastic material is too fast to be resolved by MQ NMR even at lower temperatures (considering the
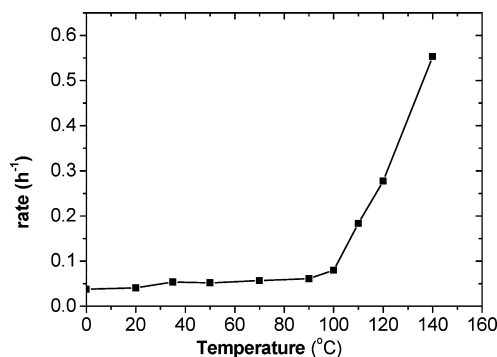

Figure 10. Storage modulus growth rate as a function of temperature. At each temperature, the rheology experiment was performed at a frequency of 1 rad/s and 0.5% strain for about 3 h.

~1 h experimental time). However, this buildup is mainly responsible for the early stage changes in the mechanical properties, which have been studied at lower temperature. Results for the storage modulus taken at a constant frequency of 1 rad/s are shown in Figure 9.

Already at temperatures above 110 °C, the storage modulus increases notably on the time scale of 1 h. Note that the data are restricted to the initial linear rise; the rheometer time allotted was not sufficient to observe the G' plateau after many hours. For a semiquantitative approach, the experiment was performed at different temperatures, each for about 3 h. We define a storage modulus growth rate as

$$\nu = \frac{G'(t) - G'(0)}{tG'(0)}$$

and plot it as a function of temperature in Figure 10. Below 110 °C, the growth rate is rather small, in the range of 0.07 h^{-1}, while above 110 °C, the rate increases sharply, reaching about 0.55 h^{-1} at 140 °C. The low but finite rate below 110 °C is possibly related to the clamping of the sample specimen inducing an artifact of the measurement. We note that the modulus growth rate decreases at much longer aging times, where the sample starts to undergo more complex changes, as reflected in the results in Figure 8b.

To obtain an initial molecular insight into the aging process, we compare high-resolution ^{1}H MAS spectra of normal SHR and a high-temperature aged sample in Figure 11. Perdeu-
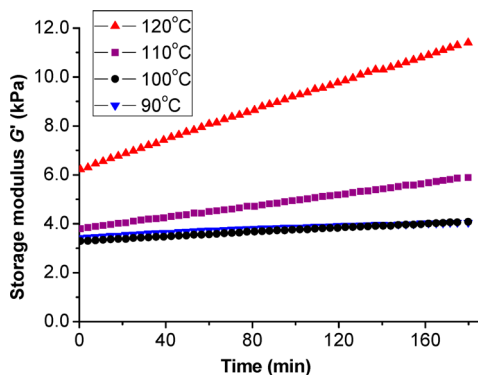

Figure 9. Storage modulus as a function of time at different temperatures with oscillation rates of 1 rad/s and 0.5% strain amplitude.
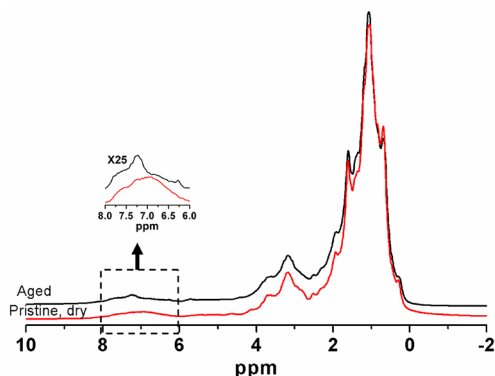
Figure 11. [1]H high-resolution MAS spectra of a pristine dry and an aged SHR sample at room temperature, spinning at 5 kHz. Both samples were swollen 2.5 times by weight in perdeuterated chloroform to increase mobility and thus spectral resolution.

terated chloroform was used to swell both samples to a weight ratio of about 2.5 to increase the molecular mobility and achieve a higher spectral resolution. All peaks are basically identical except for the region around 7 ppm, which is ascribed to protons involved in hydrogen bonds in the normal SHR. However, for the aged sample, the signal group is shifted to low field (about 7.3 ppm) and changes its shape, implying a deshielding. Importantly, the integral of the signal appears conserved, showing negligible loss of water or other species with resonances in this region.

We take this observation as qualitative evidence of chemical changes in the sample. As shown in Leibler's work,[3] different side reactions may occur if the conditions at preparation are not optimal. Herein, the high-temperature aging here may embody similar side reactions. With the presented experiments, we mainly prove the existence of chemical cross-links and entropically elastic chains, but at present we cannot deduce details of their chemical nature. Higher resolution ^{1}H and possibly ^{13}C MAS NMR studies would be needed.

Finally, we performed equilibrium-swelling studies with other solvents and solvent mixtures. Our results revealed that pristine SHR is in fact soluble in a chloroform/methanol mixture; however, the aged sample did not dissolve in this mixture even after several months but attained a constant equilibrium swelling weight ratio of about 8, again suggesting the presence of chemical cross-links in the aged sample.

CONCLUSIONS

We have presented a detailed investigation on the heterogeneous nature and the hydrogen-bonding dynamics of a popular supramolecular self-healing rubber as well as its aging properties. As revealed by proton time-domain NMR, the self-healing rubber can be treated as a nanophase-separated two-component system with a more mobile part comprising about 15% of the total sample. High-resolution MAS spectra revealed that this part is composed mainly of the saturated parts of the fatty acid chains. The 85% majority fraction comprising hydrogen-bonding moieties and associated aliphatic regions is less mobile and undergoes a glass transition below room temperature. In-depth MQ NMR studies revealed further inhomogeneity in the majority phase upon heating above T_g, suggesting a rather complex material. On the basis of IR experiments, we found that water in the self-healing rubber not

only acts as a simple plasticizer of the majority phase but also changes its hydrogen-bond structure and dynamics.

Rheology studies, low-resolution MQ NMR spectroscopy, high-resolution proton spectra, and equilibrium swelling experiment results confirmed an aging phenomenon taking place above 110 °C, which leads to irreversible chemical changes and the appearance of truly elastically active network chains and a clear plateau storage modulus in a range between 80 and 130 °C. The self-healing ability of the aged rubber was found to be significantly weakened.

We conclude by stressing that the investigated self-healing rubber is an unusual material in the sense that unlike common elastomers, it is not far above its glass transition at its common ambient operating temperature, but still in the range of ongoing strong segmental and thus mechanical relaxations in the hertz to kilohertz range, with the loss modulus being as high as its storage modulus. Only the aged material exhibits a high-temperature rubber−elastic plateau and comparably negligible dissipation.

■ AUTHOR INFORMATION

Corresponding Author
*E-mail: kay.saalwaechter@physik.uni-halle.de (K.S.); spclbh@nankai.edu.cn (P.S.).

Notes
The authors declare no competing financial interest.

■ REFERENCES

(1) van Gemert, G. M. L.; Peeters, J. W.; Söntjens, S. H. M.; Janssen, H. M.; Bosman, A. W. Self-healing supramolecular polymers in action. *Macromol. Chem. Phys.* **2012**, *213*, 234−242.

(2) Cordier, P.; Tournilhac, F.; Soulie-Ziakovic, C.; Leibler, L. Self-healing and thermoreversible rubber from supramolecular assembly. *Nature* **2008**, *451*, 977−980.

(3) Montarnal, D.; Cordier, P.; Soulié-Ziakovic, C.; Tournilhac, F.; Leibler, L. Synthesis of self-healing supramolecular rubbers from fatty acid derivatives, diethylene triamine, and urea. *J. Polym. Sci., Part A: Polym. Chem.* **2008**, *46*, 7925−7936.

(4) Sottos, N. R.; Moore, J. S. Materials chemistry: spot-on healing. *Nature* **2011**, *472*, 299−300.

(5) Chen, Y.; Kushner, A. M.; Williams, G. A.; Guan, Z. Multiphase design of autonomic self-healing thermoplastic elastomers. *Nat. Chem.* **2012**, *4*, 467.

(6) Wool, R. P. Self-healing materials: a review. *Soft Matter* **2008**, *4*, 400−418.

(7) White, S. R.; Sottos, N. R.; Geubelle, P. H.; Moore, J. S.; Kessler, M. R.; Sriram, S. R.; Brown, E. N.; Viswanathan, S. Autonomic healing of polymer composites. *Nature* **2001**, *409*, 794−797.

(8) Wu, D. Y.; Meure, S.; Solomon, D. Self-healing polymeric materials: A review of recent developments. *Prog. Polym. Sci.* **2008**, *33*, 479−522.

(9) Chen, X.; Dam, M. A.; Ono, K.; Mal, A.; Shen, H.; Nutt, S. R.; Sheran, K.; Wudl, F. A thermally re-mendable cross-linked polymeric material. *Science* **2002**, *295*, 1698−1702.

(10) Bergman, S. D.; Wudl, F. Mendable polymers. *J. Mater. Chem.* **2008**, *18*, 41−62.

(11) Chen, X.; Wudl, F.; Mal, A. K.; Shen, H.; Nutt, S. R. New thermally remendable highly cross-linked polymeric materials. *Macromolecules* **2003**, *36*, 1802−1807.

(12) Burattini, S.; Greenland, B. W.; Merino, D. H.; Weng, W.; Seppala, J.; Colquhoun, H. M.; Hayes, W.; Mackay, M. E.; Hamley, I. W.; Rowan, S. J. A healable supramolecular polymer blend based on aromatic π−π stacking and hydrogen-bonding interactions. *J. Am. Chem. Soc.* **2010**, *132*, 12051−12058.

(13) Burnworth, M.; Tang, L.; Kumpfer, J. R.; Duncan, A. J.; Beyer, F. L.; Fiore, G. L.; Rowan, S. J.; Weder, C. Optically healable supramolecular polymers. *Nature* **2011**, *472*, 334−337.

(14) Maes, F.; Montarnal, D.; Cantournet, S.; Tournilhac, F.; Corte, L.; Leibler, L. Activation and deactivation of self-healing in supramolecular rubbers. *Soft Matter* **2012**, *8*, 1681−1687.

(15) Montarnal, D.; Tournilhac, F.; Hidalgo, M.; Couturier, J.-L.; Leibler, L. Versatile one-pot synthesis of supramolecular plastics and self-healing rubbers. *J. Am. Chem. Soc.* **2009**, *131*, 7966−7967.

(16) Mauri, M.; Thomann, Y.; Schneider, H.; Saalwächter, K. Spin-diffusion NMR at low field for the study of multiphase solids. *Solid State Nucl. Magn. Reson.* **2008**, *34*, 125−141.

(17) Papon, A.; Saalwächter, K.; Schäler, K.; Guy, L.; Lequeux, F.; Montes, H. Low-field NMR Investigations of nanocomposites: polymer dynamics and network effects. *Macromolecules* **2011**, *44*, 913−922.

(18) Bärenwald, R.; Champouret, Y.; Saalwächter, K.; Schäler, K. Determination of chain flip rates in poly(ethylene) crystallites by solid-state low-field ^{1}H NMR for two different sample morphologies. *J. Phys. Chem. B* **2012**, *116*, 13089−13097.

(19) Saalwächter, K. Proton multiple-quantum NMR for the study of chain dynamics and structural constraints in polymeric soft materials. *Prog. Nucl. Magn. Reson. Spectrosc.* **2007**, *51*, 1−35.

(20) Saalwächter, K.; Herrero, B.; López-Manchado, M. A. Chain order and cross-link density of elastomers as investigated by proton multiple-quantum NMR. *Macromolecules* **2005**, *38*, 9650−9660.

(21) Chassé, W.; Valentín, J. L.; Genesky, G. D.; Cohen, C.; Saalwächter, K. Precise dipolar coupling constant distribution analysis in proton multiple-quantum NMR of elastomers. *J. Chem. Phys.* **2011**, *134*, 044907.

(22) Fechete, R.; Demco, D. E.; Blümich, B. Segmental anisotropy in strained elastomers by ^{1}H NMR of multipolar spin states. *Macromolecules* **2002**, *35*, 6083−6085.

(23) Baum, J.; Pines, A. NMR studies of clustering in solids. *J. Am. Chem. Soc.* **1986**, *108*, 7447−7454.

(24) Wang, M.; Bertmer, M.; Demco, D. E.; Blümich, B.; Litvinov, V. M.; Barthel, H. Indication of heterogeneity in chain-segment order of a PDMS layer grafted onto a silica surface by ^{1}H multiple-quantum NMR. *Macromolecules* **2003**, *36*, 4411−4413.

(25) Anderson, P. W.; Weiss, P. R. Exchange narrowing in paramagnetic resonance. *Rev. Mod. Phys.* **1953**, *25*, 269−276.

(26) Saalwächter, K.; Klüppel, M.; Luo, H.; Schneider, H. Chain order in filled SBR elastomers: a proton multiple-quantum NMR study. *Appl. Magn. Reson.* **2004**, *27*, 401−417.

(27) Lange, F.; Schwenke, K.; Kurakazu, M.; Akagi, Y.; Chung, U.-i.; Lang, M.; Sommer, J.-U.; Sakai, T.; Saalwächter, K. Connectivity and structural defects in model hydrogels: A combined proton NMR and Monte Carlo simulation study. *Macromolecules* **2011**, *44*, 9666−9674.

(28) Şerbescu, A.; Saalwächter, K. Particle-induced network formation in linear PDMS filled with silica. *Polymer* **2009**, *50*, 5434−5442.

(29) Tracht, U.; Wilhelm, M.; Heuer, A.; Feng, H.; Schmidt-Rohr, K.; Spiess, H. W. Length scale of dynamic heterogeneities at the glass transition determined by multidimensional nuclear magnetic resonance. *Phys. Rev. Lett.* **1998**, *81*, 2727−2730.

(30) Saalwächter, K.; Heuer, A. Chain dynamics in elastomers as investigated by proton multiple-quantum NMR. *Macromolecules* **2006**, *39*, 3291−3303.

(31) Noro, A.; Matsushita, Y.; Lodge, T. P. Thermoreversible supramacromolecular ion gels via hydrogen bonding. *Macromolecules* **2008**, *41*, 5839−5844.

(32) Choperena, A.; Painter, P. Hydrogen bonding in polymers: effect of temperature on the OH stretching bands of poly-(vinylphenol). *Macromolecules* **2009**, *42*, 6159−6165.

(33) Sagle, L. B.; Zhang, Y.; Litosh, V. A.; Chen, X.; Cho, Y.; Cremer, P. S. Investigating the hydrogen-bonding model of urea denaturation. *J. Am. Chem. Soc.* **2009**, *131*, 9304−9310.

(34) Guo, L.; Sato, H.; Hashimoto, T.; Ozaki, Y. FTIR study on hydrogen-bonding interactions in biodegradable polymer blends of poly(3-hydroxybutyrate) and poly(4-vinylphenol). *Macromolecules* **2010**, *43*, 3897−3902.